PHYSICAL REVIEW E VOLUME 61, NUMBER 4 APRIL 2000

# Spatiotemporal growth of faceted and curved single crystals

Thein Kyu,* Rujul Mehta, and Hao-Wen Chiu†
*Institute of Polymer Engineering, The University of Akron, Akron, Ohio 44325*

(Received 7 September 1999)

The spatiotemporal growth of single crystals in a crystalline polymer has been investigated theoretically based on a nonconserved time dependent Ginzburg-Landau equation (known as TDGL model A). In the description of the total free energy, a double-well local free energy density signifying metastability of crystal ordering is combined with a nonlocal free energy term representing an interface gradient. The resulting nonlinear reaction diffusion equation after renormalization possesses a solitary wave property. Two-dimensional numerical calculations were performed to elucidate the faceted single crystal growth including square, rectangular, diamond-shaped, and curved single crystals. A three-dimensional simulation was also undertaken for the emergence of diamond-shaped single crystals in polyethylene. Of particular importance is that the model field parameters can be linked directly to the material parameters of polyethylene single crystals. Simulation with various elements of the interface gradient coefficient tensor captures various topologies of polymer single crystals.

PACS number(s): 61.41.+e, 81.10.Aj, 87.15.Nn

## I. INTRODUCTION

A rich variety of polymer morphologies ranging from single crystals to spherulites have been reported over a half century [1–4]. The former have been generally grown from polymer solution, whereas the latter are commonly observed during crystallization from the melt by either isothermal crystallization or cooling below the crystallization temperature. Recently, it has become apparent that some polymer single crystals can be grown from the melt as well [5]. The wealth of experimental evidence on polymer morphology and crystallization kinetics is appealing for theoretical development. However, these morphologies are kinetically solidified, and thereby nonequilibrium in nature. It is difficult to rationalize all these nonequilibrium structures in a coherent manner without understanding how these structures emerge during isothermal crystallization. Hence it is essential to investigate the spatiotemporal growth of crystalline textures. Numerous theoretical efforts have been directed to the elucidation of crystallization habits and emerging morphologies of semicrystalline polymers; however, a unified opinion has yet to emerge, particularly a theoretical elucidation of the polymer crystal growth [6–14].

One of the most tested theories in polymer crystallization is the Lauritzen-Hoffman (LH) nucleation theory, which describes the deposition of a stem on a flat substrate and the subsequent attachment of additional stems on adjacent sides [6,7]. The original LH theory has been applied to the kinetics of rectangular and/or diamond-shaped single crystal growth with straight edges. However, it has been found experimentally that some solution grown as well as melt grown single crystals exhibit curved topologies [2,8]. Sadler pointed out a potential deficiency of the original LH theory in explaining the growth of such curved crystals [9]. Subsequently, Sadler introduced a surface roughening concept to explain the curved crystal growth, and concluded that growth sectors such as (110) and (100) planes grow at different rates, thereby resulting in curved single crystals. Miller and Hoffman [11,12] contended that the faces in polyethylene single crystal lamellae exhibiting curvature are the slowly growing (100) plane, but not the fast growing (110) front. They modified the nucleation theory with the idea that the growth in the (110) sector is governed by the flat edge mechanism as proposed in the original LH model, but the growth at the (100) front takes place as serrated on the molecular level.

Mansfield [10] calculated the nucleation of a stem on an existing flat substrate and subsequent spreading events based on the continuum approach originally proposed by Frank [13] using the moving boundary equation. The Mansfield model captured the growth behavior of regime II (a multinucleation regime) and regime III (a multinucleation regime with rough surfaces) with various spatial growth topologies including lozenges and curved single crystals, but it cannot account for the growth in the mono-nucleation regime (i.e., the so-called regime I). Tanzawa and Toda [14] simulated various single crystal topologies based on the Mansfield model using a Monte Carlo approach. They concluded that their simulation conforms remarkably well to the theoretical expression of Mansfield [10]. However, Point and Villers [15] argued that Mansfield's solution is not exact, and is incapable of explaining curved (100) crystals of large extension ratios. They proposed a unified model that mediated between the nucleation-controlled growth and the surface roughening mechanism. Their computation based on the modified Frank equation in conjunction with Sadler's surface roughening conditions captured the highly elongated curved crystals as well as the bisectorization of lanceolated crystals observed experimentally in Ref. [16]. The original LH theory [6,7] and its modifications [11,12], as well as the alternative models [9,10,14,15], have their own merits in explaining various crystallization habits, but an agreed upon opinion has yet to emerge [5].

---

*Author to whom correspondence should be addressed. Electronic address: tkyu@uakron.edu

†Present address: Gentex Optics, R&D Materials Division, Dudley, MA 01571.

The original LH kinetic theory describes a temporal crystal growth, but it lacks spatial diffusion of the interface. Hence most simulations pertaining to the spatiotemporal growth of polymer single crystals utilize the classical Frank model [13] that involves calculations with a moving front having a crystal-melt interface of zero thickness. Such a moving front with a discrete interface often leads to mathematical complications [13]. To circumvent the moving boundary problem, it is advantageous to employ front propagation with a crystal-melt interface of nonzero thickness or a finite interface gradient such as propagation of interface in the form of a solitary wave [17], but with an appropriate free energy to capture the physical essence of crystallization.

We proposed a ‘‘phase field’’ model in which the entire spatial field is treated in the context of a time dependent ‘‘phase’’ order parameter, which describes the local state (or phase) of the system in time and space [18–25]. It is thus possible to express the entire system as a continuous field with thermodynamic variables as a function of the phase order parameter. Such a model eliminates the sharp edges of the interface inherent in the moving boundary approach [13], and thus can be solved numerically. The phase field model derived from the coupled time-dependent Ginzburg-Landau (TDGL) model C [26,27] has been successfully applied to the crystal growth in metal alloys [23] and eutectic crystal growth [28]. Recently, a similar methodology was applied to the elucidation of rhythmic growth of concentric and spiral spherulites in a binary polymer blend containing a crystalline polymer as one component [29]. In model C, the conserved compositional order parameter (concentration or volume fraction of the blend) and the nonconserved crystal order parameter are coupled in nonlinear reaction diffusion equations [23,28,29]. The total free energy density involves a Landau type double well potential with respect to the crystal order parameter for crystallization [29] and a Flory-Huggins free energy density for a demixing of the blend [30]. For a single component system, the nonlinear differential equation involving the conserved compositional order parameter becomes unnecessary. Hence, the two-coupled TDGL (model C) equations can be reduced to a single nonlinear TDGL (model A) equation with a nonconserved order parameter pertaining to crystallization, hereafter called a crystal order parameter. Note that for a more complex case where the free energy functionals for density and orientational crystal order parameters are different, the two coupled model A equations of the individual order parameters may be employed. In addition, all sharp interface problems have been shown to arise as a particular limit of the phase field [20]. In the dendritic growth of snowflakes [22], it is necessary to couple with the heat balance equation in the phase field model. However, the mass diffusion of polymer molecules is extremely slow relative to the heat flux, such that the temperature field can be regarded as uniform during isothermal crystallization. Hence the effect of heat balance coupling on the emerging polymer crystals, if any, would be negligible.

In this paper, we deduce a theoretical model based on the TDGL model A by taking into consideration a double well potential with respect to a crystal order parameter [22] to capture the metastability of the polymer melt subjected to crystallization. The total free energy is composed of a nonlocal gradient term and a local free energy density that is expanded in terms of the crystal order parameter. The resulting nonlinear reaction diffusion equation can be solved numerically on a square lattice $(256\times256)$ using a finite difference method for spatial steps, and an explicit method for temporal steps with an absorbing boundary condition. The simulation has been performed using various temporal steps $(\Delta t)$ on several grids $(64\times64$, $128\times128$, $256\times256$, and $512\times512)$ to assure stability of the computation; however, only the results of $(256\times256)$ for two-dimensional (2D) and $(64\times64\times64)$ for 3D simulations are shown here to avoid cumbersome calculation. The spatiotemporal growth of various forms of polymer single crystals has been demonstrated and subsequently compared with the diamond-shaped polyethylene single crystals using the literature values for materials parameters involved.

## II. THEORETICAL SCHEME

The time-dependent Ginzburg-Landau equation is basically an equation of motion that relates the temporal change of a phase order parameter (e.g., a local concentration) to a local chemical potential and a nonlocal interface gradient. The TDGL model A equation for a nonconserved order parameter is customarily expressed as [26,27]

$$\frac{\partial\psi(r,t)}{\partial t}=-\Gamma\frac{\delta F}{\delta\psi}, \tag{1}$$

where $\psi$ represents the crystal order parameter, and $\Gamma$ is the mobility. $F$ is the total free energy of the crystal ordering, which may be defined as

$$F(\psi)=\int f_{\mathrm{cryst}}(\psi)d\Omega, \tag{2}$$

where the total free energy of the crystal ordering consists of a local free energy density and a nonlocal gradient term, i.e., $f_{\mathrm{cryst}}=f_{\mathrm{local}}+f_{\mathrm{grad}}$. The local free energy density in turn may be given in the form of the Landau expansion as [23,25,29]

$$f_{\mathrm{local}}(\psi)=W\int_0^{\psi}\psi(\psi-1)\left(\psi-\frac{1}{2}-\theta(T)\right)d\psi=W\left[\zeta(T)\frac{\psi^2}{2}\right.$$
$$\left.-[1+\zeta(T)]\frac{\psi^3}{3}+\frac{\psi^4}{4}\right], \tag{3}$$

where $\zeta(T)=1/2+\theta(T)$, and $W$ is a dimensionless constant. As will be demonstrated in a later section, $|\zeta(T)|$ is a quantity that can be related to supercooling and heat of fusion. As shown in Fig. 1, the local free energy density has a double well shape with respect to the crystal order parameter $\psi$. Physically, $\psi=0$ represents the melt, whereas $\psi>\zeta$ implies a crystalline state. At the crystal melting temperature $T_m$, the free energy densities for the crystalline state and the melt are equivalent. When $T<T_m$, the free energy density of the crystal ordering has a global minimum at $\psi=1$. The solid crystal phase is therefore a stable phase as it has the lowest free energy, and thus the melt is metastable. On the other hand, when $T>T_m$, the global minimum of the free energy density is at $\psi=0$, which represents a stable melt; thus all crystals must melt.

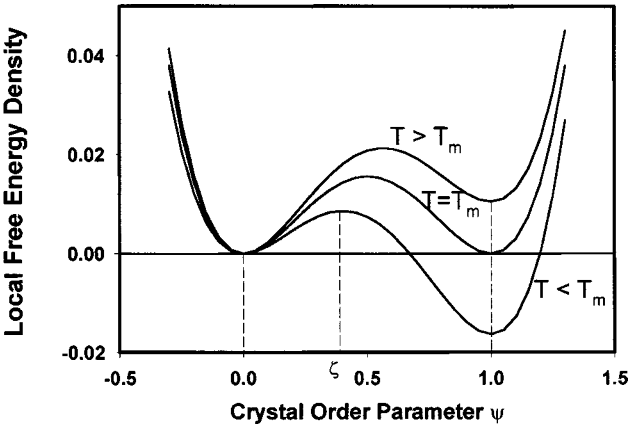

FIG. 1. Schematic plot of the local free energy density and crystal order parameter $\psi$ for various temperatures showing the metastable energy barrier for a phase transition from the melt ($\psi=0$) to the crystalline state ($\psi=1$) with equilibrium at $T_m$.

The nonlocal free energy density may be described in terms of the gradient free energy density as

$$f_{\text{grad}}(\psi)=\frac{1}{2}[\boldsymbol{\kappa}\cdot\nabla\psi]^2, \tag{4}$$

where $\boldsymbol{\kappa}$ is the interface gradient coefficient, and $\nabla$ is the space derivative operator. In order to take into account the surface energetic at two growth fronts, we consider $\boldsymbol{\kappa}$ as a second rank tensor [31], i.e.,

$$\boldsymbol{\kappa}=\begin{Bmatrix}\kappa_{11} & \kappa_{12}\\ \kappa_{21} & \kappa_{22}\end{Bmatrix}. \tag{5}$$

It should be noted that the tensorial representation of $\boldsymbol{\kappa}$ was originally proposed by Cahn and Hilliard, but it was treated as scalar for simplicity in their original paper [31].

Substituting Eqs. (2)–(5) into Eq. (1), one obtains

$$\frac{\partial\psi}{\partial t}=-\Gamma\frac{\delta F}{\delta\psi}=-\Gamma[W\psi(\psi-1)(\psi-\zeta)-\nabla\cdot\{\boldsymbol{\kappa}\cdot(\boldsymbol{\kappa}\cdot\nabla\psi)\}]. \tag{6}$$

The derivation of the functional derivative $\delta F/\delta\psi$ in Eq. (6) is given in the Appendix. It is customary to express the above equation in a dimensionless form with dimensionless time $\tau$ and dimensionless variables denoted with tilde symbols as follows:

$$\tilde{x}=\frac{x}{l^*},\quad \tilde{y}=\frac{y}{l^*},\quad \tau=\frac{D}{l^{*2}}t; \tag{7}$$

where $l^*$ is the characteristic length, and $D$ is the diffusion coefficient. Substituting Eq. (7) into Eq. (6) leads to the final governing equation as

$$\frac{\partial\psi}{\partial\tau}=-\tilde{\Gamma}[W\psi(\psi-1)(\psi-\zeta)-\tilde{\boldsymbol{\nabla}}\cdot\{\tilde{\boldsymbol{\kappa}}\cdot(\tilde{\boldsymbol{\kappa}}\cdot\tilde{\boldsymbol{\nabla}}\psi)\}], \tag{8}$$

where $\tilde{\Gamma}=\Gamma l^{*2}/D$, $\tilde{\kappa}_{ij}=\tilde{\kappa}_{ij}/l^*$, and $\tilde{\boldsymbol{\nabla}}=(\partial/\partial\tilde{x})\hat{e}^x+(\partial/\partial\tilde{y})\hat{e}^y$; $\hat{e}^x$ and $\hat{e}^y$ being covariant unit vectors in $x$ and $y$ directions.

## III. RESULTS AND DISCUSSION

### A. Faceted single crystals

Faceted single crystals in polymers are essentially thin layer lamellar crystals [1]. Although simplified in many aspects, this rendition of a planar two-dimensional lamellar crystal serves as a basis for elucidating various fundamental features that pertain to the emergence of morphology of bulk polymer crystals. The lateral growth in the lamellar crystal may be viewed as the addition of fresh stems that reflects the unit cell geometry of the polymer crystal [1–5]. The lamellar crystals have well defined shapes predominantly in rectangular or truncated rectangular shapes. However, for the purpose of demonstration, we shall first consider the simplest case of isotropic growth, i.e., equal growth rates along the two lateral edges that give rise to a square single crystal [32]. The elements of the interface gradient coefficient tensor in dimensionless units may be taken as $\tilde{\kappa}_{11}=\tilde{\kappa}_{22}=\tilde{\kappa}$ and $\tilde{\kappa}_{12}=\tilde{\kappa}_{21}=0$ which, when combined with Eq. (8), lead to

$$\frac{\partial\psi}{\partial\tau}=-\tilde{\Gamma}[W\psi(\psi-1)(\psi-\zeta)-\tilde{\kappa}^2\tilde{\nabla}^2\psi]. \tag{9}$$

It is well established that nucleation can be triggered through generation of strong thermal noise or seeded with a foreign object. In the present case, a nucleation event is triggered with a single nucleus at the center of the lattice having a Gaussian profile such that $\psi(r)=\exp(-r^2/R^2)$, $R$ being the radius of the initial nucleus [33]. It should be pointed out that the nucleus could be of any shape, for instance in the form of thermal noise, as it is inconsequential to the spatiotemporal growth of a single crystal. That is to say the crystal spreads along a given substrate by depositing new stems on adjacent sides and eventually emerges to a square shape (Fig. 2), although the crystallization begins with a round nucleus.

Figure 3 shows the detailed growth events of the same single crystal over a short time span in which a new stem is deposited at a lamellar front that constitutes surface nucleation. In this nucleation event, excess surface free energy is created while the bulk free energy decreases due to growth. The additional stems are attached in adjacent positions on each side, and spread in both directions along the lateral strip. The lateral spreading of the stems may be characterized as lateral growth with a rate $g$, which occurs on all four sides. This lateral growth is analogous to the substrate completion process in regime I [7,10]. The fact that the growth along the lateral edge is favored over the growth normal to it is simply due to the high cost of the nucleation process. The formation of a new strip (nucleation) may be viewed as the growth normal to the lateral edge which is usually characterized as the nucleation-controlled growth with a rate denoted $G$. It is apparent that the growth rate along the lateral edge, $g$ is greater than that normal to it, $G$. However, a new nucleation event could occur before all lateral sites are completely filled, in particular when the crystal size becomes very large. Strictly speaking, the present finding is at variance with the classical picture of regime I, where all sites must be completely filled before a new nucleation could occur on the just completed strip. It is also different from regime II, where more than two nuclei can form on the same strip [5,10].

Figure 4(a) shows the temporal change of the crystal size

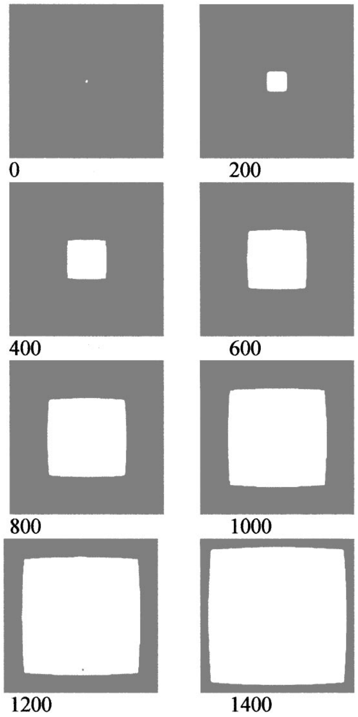

FIG. 2. The emergence of the square single crystal in the crystal order parameter field calculated according to Eq. (7), with $\tilde{\Gamma}=0.1894$, $W=5.086$, $\zeta=0.256$, and $\tilde{\kappa}^2=0.1063$ on a $256\times256$ lattice, showing the temporal increase in the single crystal size.

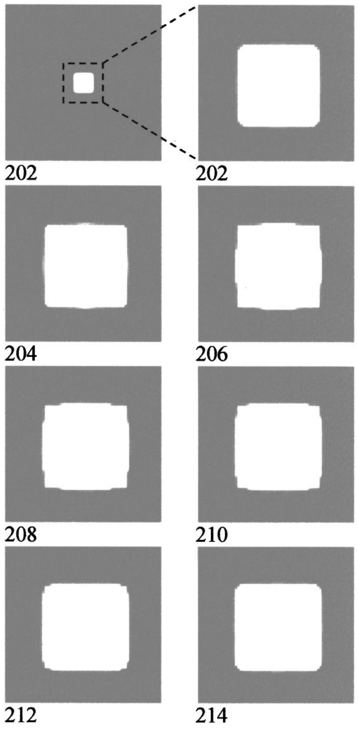

FIG. 3. The enlarged version of the emerging single crystal of Fig. 2, at an interval of 202–214 time steps, exhibiting surface nucleation on four sides (see 204) followed by spreading of the stems along the edges (204–214).

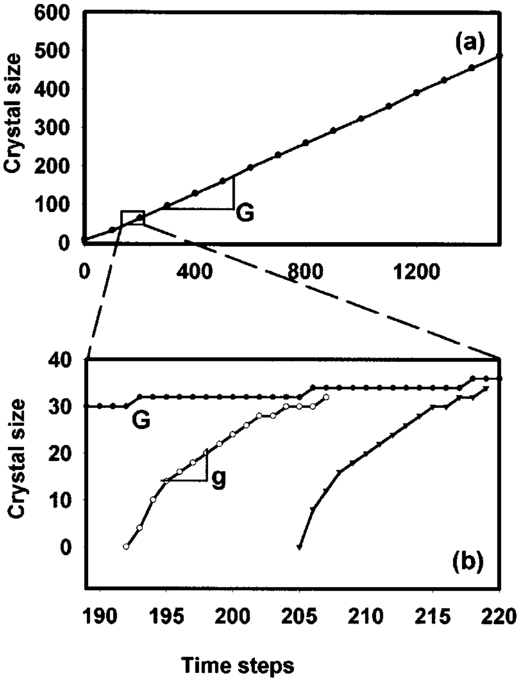

FIG. 4. The variation of the single crystal size with time steps; showing (a) apparent linear growth with a nucleation controlled growth rate $G$ over a time scale corresponding to Fig. 2; and (b) a change in dimension of the single crystal across the center with a growth rate $G$ and along the lateral edge, with a lateral growth rate $g$ over a shorter time span corresponding to Fig. 3.

over a long time. The detailed growth behavior may be best characterized in comparison with the lateral growth (spreading of the stems) along the strip in a shorter time span [Fig. 4(b)]. The initial increase of the crystal size is due to the attachment of a new stem on the strip representing surface nucleation. The crystal size remains unchanged until the entire edge has been filled, then the size increases by an amount of the width of a single stem in the second nucleation event. The lateral growth along the strip exhibits a nonlinear (sigmoidal-like) growth during stem propagation. However, if the crystal size were sufficiently large, the growth curve will be stretched out such that the intermediate interval may be approximated by a linear slope to roughly estimate the lateral growth rate $g$. The lateral growth slows down asymptotically when the spreading is near completion, as shown in Fig. 4(b). Then the crystal size increases again during the subsequent nucleation cycle. Of particular interest is that the present calculation captures the square single crystal as observed in poly (4-methyl-pentene-1) [32], although pattern matching is not the main objective of the present study.

As expected, the overall decay of free energy with time appears monotonic [Fig. 5(a)]. However, if one carefully examines the intricate details of the free energy dissipation during the individual events of nucleation and growth as exemplified in Fig. 5(b), the free energy decays in a rhythmic manner with time. This observation is not surprising in view of the fact that the surface nucleation generates excess free energy; thus it raises the bulk free energy periodically whenever a new nucleation event occurs. Consequently, the resultant free energy curve shows a rhythmic character, i.e., the free energy humps appear periodically by overlapping on the montonically decaying free energy. Of particular importance

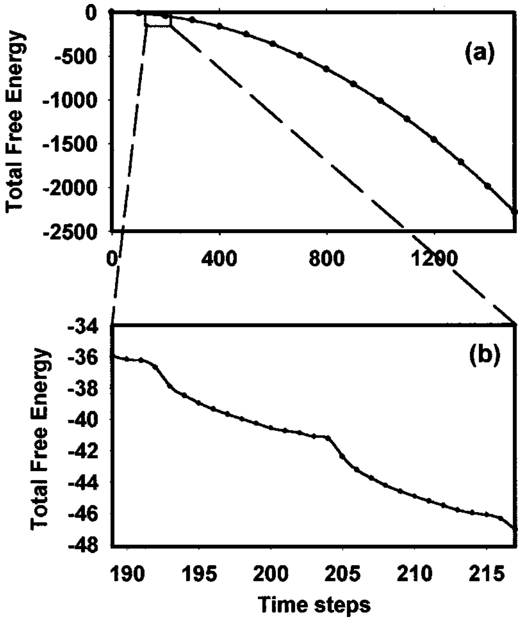

FIG. 5. The free energy dissipation during the course of crystallization showing (a) a monotonous decay over the long time scale corresponding to Fig. 4(a); and (b) a discontinuity in the free energy curve caused by the excess free energy due to successive surface nucleation events taking place on a shorter time span corresponding to Fig. 4(b).

is that this rhythmic energy dissipation occurs in synchronism with the successive surface nucleation followed by the lateral growth.

In practice, different faceted fronts grow with different rates. Hence the single crystals thus formed would have different shapes such as rectangular or diamond shapes. Lotz, Lovinger, and Cais [34] found that syndiotactic polypropylene (*s*-PP) single crystals grown from the melt have an orthorhombic unit cell with dimensions $a=1.45\,\mathrm{nm}$, $b=1.12\,\mathrm{nm}$, and $c=0.74\,\mathrm{nm}$. Apparently, the growth along the (010) plane is greater than that of the (100) front; therefore, the *s*-PP single crystal is highly anisotropic showing a lathelike (rectangular) appearance with the long axis along the *b*-axis direction and the short axis along the *a*-axis direction. Later, Bu *et al.* [35] showed that the *s*-PP single crystals often exhibit sectorization along the diagonals in which two pairs of microsectors are seemingly twinned. Further investigation using atomic force microscopy and electron diffraction revealed that the lamellar thickness in the two sectors is different, showing different folding habits. These observed textures have been ascribed to result from the different fold energies in the two sectors [36].

To obtain a lathelike single crystal, the elements of the interface gradient coefficient tensor in dimensionless units may be set as $\tilde{\kappa}_{11}\neq\tilde{\kappa}_{22}$ and $\tilde{\kappa}_{12}=\tilde{\kappa}_{21}=0$. Substituting in Eqs. (5) and (6), one obtains

$$\frac{\partial\psi}{\partial\tau}=-\tilde{\Gamma}\left[W\psi(\psi-1)(\psi-\zeta)-\left(\tilde{\kappa}_{11}^{2}\frac{\partial^{2}\psi}{\partial\tilde{x}^{2}}+\tilde{\kappa}_{22}^{2}\frac{\partial^{2}\psi}{\partial\tilde{y}^{2}}\right)\right]. \tag{10}$$

Figure 6 shows the simulated rectangular single crystals based on Eq. (8) with different values of $\tilde{\kappa}_{11}$ and $\tilde{\kappa}_{22}$, inferring the relative growth rates in two different directions. As surface nucleation occurs before the lateral growth along the entire strip has been completed, the longer side of the single crystal appears serrated on the molecular level and curved, but it is flat and smooth on the shorter side. If the growth rate *G* were sufficiently small (i.e., in regime I), the pattern would resemble the lathelike single crystal similar to that observed in the *s*-PP single crystals [35,36].

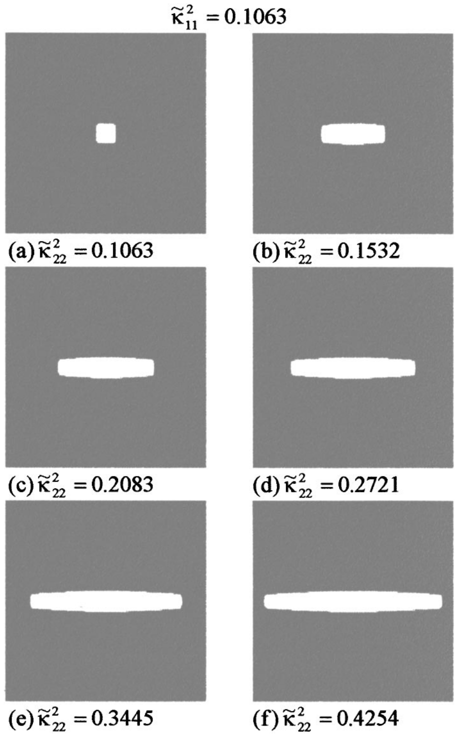
$\tilde{\kappa}_{11}^2 = 0.1063$

(a) $\tilde{\kappa}_{22}^2 = 0.1063$ (b) $\tilde{\kappa}_{22}^2 = 0.1532$

(c) $\tilde{\kappa}_{22}^2 = 0.2083$ (d) $\tilde{\kappa}_{22}^2 = 0.2721$

(e) $\tilde{\kappa}_{22}^2 = 0.3445$ (f) $\tilde{\kappa}_{22}^2 = 0.4254$

FIG. 6. Various rectangular single crystals calculated based on Eq. (10) using $\tilde{\Gamma}=0.1894$, $W=5.086$, $\zeta=0.256$, and $\tilde{\kappa}_{11}^{2}=0.1063$, with various values of $\tilde{\kappa}_{22}^{2}$: (a) 0.1063, (b) 0.1532, (c) 0.2083, (d) 0.2721, (e) 0.3445, and (f) 0.4254.

In Figs. 7(a)–7(d) we show the effect of *W* values on the emerging patterns of the single crystals. Basically increasing *W* value corresponds to reducing the individual values of $\tilde{\kappa}_{11}$ and $\tilde{\kappa}_{22}$, keeping their ratio constant. Physically *W* serves as a factor to alter the steepness of the nucleation barrier. The larger the *W* value, the steeper the barrier, and thereby the harder it is for the surface nucleation to occur. This in turn implies that the surface nucleation rate *G* would be much smaller relative to the lateral growth rate *g*. At a certain large *W* value for a given set of $\tilde{\kappa}_{11}$ and $\tilde{\kappa}_{22}$, the crystal would eventually cease to grow in the direction normal to the longer side. When this occurs, the calculated patterns [Fig. 7(d)] resemble a thin lathelike single crystal. On the other hand, when the *W* value is reduced, the curvature in the longer side would become more pronounced due to the increase in the surface nucleation rate [Fig. 7(a)]. At intermediate values of *W*, the barrel (truncated curved texture) to axial-like patterns would emerge [Figs. 7(b) and 7(c)].

### B. Application to diamond-shaped single crystals in polyethylene

#### 1. *Crystallographic representation*

As is well known, the unit cell of polyethylene (PE) crystal is orthorhombic with cell dimensions of $a=0.736\,\mathrm{nm}$, $b$

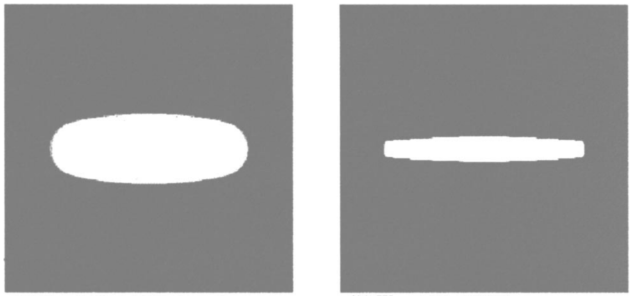
(a) $W = 2.54$ at 1450 time steps (b) $W = 5.09$ at 1000

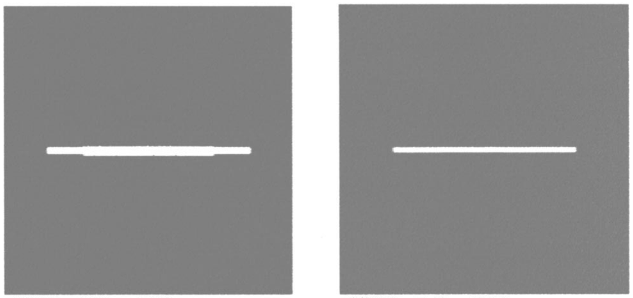
(c) $W = 5.35$ at 1250 (d) $W = 7.62$ at 1000.

FIG. 7. The calculated single crystal patterns in the crystal order parameter field showing various textures ranging from oval to needlelike shapes. The calculation was undertaken according to Eq. (10), using $\tilde{\Gamma}=0.1894$, $\tilde{\kappa}_{11}^2=0.1063$, $\tilde{\kappa}_{22}^2=0.4254$, and $\zeta=0.256$, with various $W$ values.

$=0.492$ nm, and $c=0.254$ nm, in which the molecular chains align parallel to the $c$ axis and on the average two chains pass through one unit cell [1]. Figure 8 depicts a rhomboidal lattice model, projected onto the (001) plane with the $x$ and $y$ axes being parallel to the $(\bar{1}10)$ and (110) planes, respectively. The angle between the $x$ and $y$ axes is $\alpha=112.5°$. The growth along the (110) plane takes places normal to both $x$ and $y$ axes, whereas the growth along the (100) takes place in perpendicular to the crystal $a$ axis.

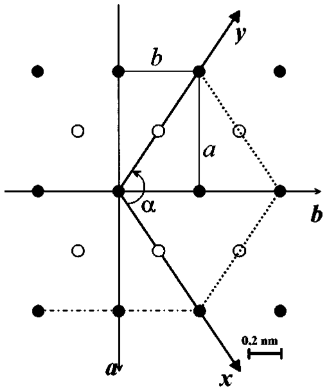

FIG. 8. A schematic representation of a polyethylene unit cell with the plane of projection perpendicular to the chain $c$ axis. The nominal crystallographic dimensions of the body centered orthorhombic unit cell are $a=0.736$ nm, $b=0.492$ nm, and $c=0.254$ nm. The filled and unfilled circles denote $CH_2$ groups in the plane and out of the plane of the paper, respectively. The solid line represents the crystallographic $a$ and $b$ axes. The rhomboidal lattice is constructed in terms of the $x$ and $y$ axes denoted by the bold solid line, with an angle of $\alpha=112.5°$. The dotted line represents the (110) growth front, whereas the dash dotted line represents the (100) growth front.

### *2. Model*

In PE single crystals the growth takes place along four sectors with growth fronts parallel to the (110) planes. In order to compute the growth of PE single crystals using the experimental data (i.e., material parameters) in real dimensions of space and time, we shall employ Eq. (6) directly. Furthermore, it is advantageous to simulate the growth of PE single crystals on a rhomboidal lattice rather than a square lattice for which Eq. (6) may be rewritten as

$$\frac{\partial\psi}{\partial t}=-\Gamma\left[W\psi(\psi-1)(\psi-\zeta)-\kappa^2\nabla^2\psi-2\cos(\alpha)\kappa^2\frac{\partial^2\psi}{\partial x\,\partial y}\right], \tag{11}$$

The detailed derivation of Eq. (11) is presented in the Appendix according to Eq. (A10).

Next, to relate the model parameters such as $W$, $\kappa$, $\Gamma$, and $\zeta$ to the material parameters, we follow the approach of Refs. [31], [37], and [23]. The excess free energy at the interface (or the surface) energy $\sigma$ may be evaluated in accordance with Cahn and co-workers' approach [31,37], i.e.,

$$\frac{\sigma}{nRT}=\int_0^1\kappa\sqrt{2f_{\mathrm{local}}}\,d\psi, \tag{12}$$

where $n$ is the molar density of the mixture. At $T=T_m$ the surface energy is given from Eq. (3) as

$$\frac{\sigma}{nRT}=\frac{\kappa}{6}\left(\frac{W}{2}\right)^{1/2}. \tag{13}$$

Further, the interfacial thickness $\delta$ is estimated as

$$\delta=\kappa\left(\frac{1}{2f_{\mathrm{local\,max}}}\right)^{1/2}. \tag{14}$$

Using Eq. (3), we obtain

$$\delta=4\kappa\left(\frac{2}{W}\right)^{1/2}. \tag{15}$$

Integrating Eq. (3), one obtains

$$\Delta f_{\mathrm{local}}=-\frac{\Delta H_u}{nRT}\left(1-\frac{T}{T_m}\right)=\frac{W}{6}\left(\zeta-\frac{1}{2}\right). \tag{16}$$

According to Harowell and Oxtoby [38], $\Gamma$ can be related to the velocity $v$ of the interface as follows:

$$v=-\frac{3}{2\sqrt{2}}\Gamma\,\delta\Delta f_{\mathrm{local}}. \tag{17}$$

Solving Eqs. (3), (13), (15), and (16), one obtains

$$W=48\frac{\sigma}{nRT}\frac{1}{\delta}, \tag{18}$$

TABLE I. Model parameters calculated based on Eqs. (17)–(20) using the material parameters listed.

| (a) Material parameters | | (b) Model parameters | |
|---|---|---|---|
| $\Delta H_u$[a] | $2.8\times10^8\ \mathrm{J\,m^{-3}}$ | $\Gamma$ | $0.034\ \mathrm{s^{-1}}$ |
| $T$ | 350 K | $\kappa^2$ | $2.149\times10^{-16}\ \mathrm{m^2}$ |
| $T_m$[a] | 387 K | $W$ | $6.878\times10^3$ |
| $v$ | $1\times10^{-8}\ \mathrm{m\,s^{-1}}$ | $\zeta$ | 0.256 |
| $\delta$ | $1\times10^{-9}\ \mathrm{m}$ | | |
| $\sigma$[a,b] | $0.0137\ \mathrm{J\,m^{-2}}$ | | |

[a] For solvated PE crystals [7].

[b] The surface energy $\sigma$ is approximated as $\sigma_l=0.0137\ \mathrm{J\,m^2}$ [7].

$$\kappa^2=\frac{3}{2}\frac{\sigma}{nRT}\delta, \tag{19}$$

$$\zeta=\frac{1}{2}-\frac{\Delta H_u}{8}\left(\frac{\delta}{\sigma}\right)\left(1-\frac{T}{T_m}\right). \tag{20}$$

The TDGL equation in Eq. (11) may be solved numerically on the rhomboidal lattice defined in terms of the $x$-$y$ coordinates as depicted in Fig. 8. The thermodynamic and fixed parameters used in Eqs. (17)–(20) are listed in Table I(a). Using $l^*=1.25$ nm and $D=5\times10^{-12}\ \mathrm{m^2/s}$, and solving Eqs. (17)–(20), we obtained the values of the reduced coefficients of Eq. (11), as listed in Table I(b).

Figure 9 shows the crystallization order parameter field manifesting the growth sequence of a diamond-shaped single crystal. A stem each is deposited on each side of the lattice, i.e., at the lateral edges of all four-crystal fronts via surface nucleation. The growth occurs rapidly by spreading along these edges. If the lateral growth along the edge is much faster than the growth normal to it, the sides of the diamond-shaped single crystals would be sharp, thus it is analogous to the regime I growth proposed by the original LH theory. However, if the surface nucleation rate is sizable relative to the lateral growth rate, a new nucleation event occurs on the advancing strip before all the sites on these lateral edges are fully filled. As shown in Fig. 9, the diamond-shaped single crystals reveal serrated rough edges on all sides. It is apparent that the present model can capture the serrated topology depending on the relative growth rates along the edge and normal to it.

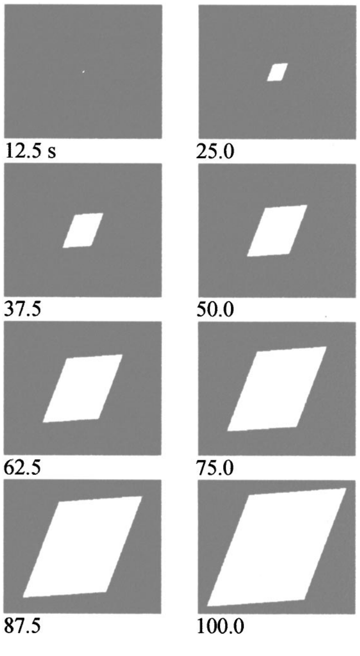

FIG. 9. The spatiotemporal growth of the diamond shaped polyethylene crystal in the crystal order parameter field calculated according to Eq. (11), with the coefficients listed in Table I.

Although polymer single crystals are essentially flat thin lamellar crystals, the crystal growth is known to be a three-dimensional problem. A natural question arises as to whether there is any difference in the single crystal growth behavior in the 2D and 3D simulations. We undertook this task for the 3D case by rewriting Eq. (11) and performing the simulation on a smaller cubic lattice (64×64×64) to avoid tedious calculation and the problem of memory overflow.

Equation (11) is modified to include the $z$ axis, which is parallel to the crystal $c$ axis and perpendicular to the $x$-$y$ plane.

$$\frac{\partial\psi}{\partial t}=-\Gamma\left[W\psi(\psi-1)(\psi-\zeta)-\kappa_{x,y}^2\left(\frac{\partial^2\psi}{\partial x^2}+\frac{\partial^2\psi}{\partial y^2}\right)\right.$$
$$\left.-\kappa_z^2\frac{\partial^2\psi}{\partial z^2}-2\cos(\alpha)\kappa_{x,y}^2\frac{\partial^2\psi}{\partial xy}\right], \tag{21}$$

The model parameters can be related to the materials parameters as follows:

$$W=48\frac{\sigma_l}{nRT}\frac{1}{\delta}, \tag{22a}$$

$$\kappa_{x,y}^2=\frac{3}{2}\frac{\sigma_l}{nRT}\delta, \tag{22b}$$

$$\kappa_z^2=\frac{3}{2}\frac{\sigma_e}{nRT}\delta, \tag{22c}$$

$$\zeta=\frac{1}{2}-\frac{\Delta H_u}{8}\left(\frac{\delta}{\sigma_l}\right)\left(1-\frac{T}{T_m}\right). \tag{22d}$$

Equation (21) was solved for a 3D growth setting $l_{x,y}^*=1.25$ nm, $l_z^*=10$ nm, and $D=5\times10^{-12}\ \mathrm{m^2/s}$, along with the material parameters listed in Table II(a). The model parameters in Table II(b) were calculated in accordance with Eqs. (22a)–(22d) using the material parameters of Table II(a). Figure 10 illustrates the cross sections in the $x$-$y$ and $x$-$z$ planes of the emerging PE single crystal calculated in three dimensions. The first column shows the top view exhibiting a diamond-shaped topology, whereas the second column manifests the side view representing the lamellar thickness. It is seen that growth occurs exclusively in the lateral direction, and virtually ceases in the thickness direction because of the high penalty for nucleation to occur on the folded lamellar surface relative to the sides. Hence the nucleation on the folded surface is highly unfavorable, leading to growth in the lateral directions; this is exactly what one observes experimentally. In practice, some crystal defects or impurities on the folded surface could act like nuclei upon which new single crystal layers can grow successively on the

TABLE II. Model parameters calculated based on Eqs. (22a)–(22d), using the material parameters listed.

| (a) Material parameters | | (b) Model parameters | |
|---|---|---|---|
| $\Delta H_u{}^{\mathrm{a}}$ | $2.8\times10^{8}$ J m$^{-3}$ | $\Gamma$ | 0.034 s$^{-1}$ |
| $T$ | 350 K | $\kappa_{x,y}^2$ | $2.149\times10^{-16}$ m$^2$ |
| $T_m{}^{\mathrm{a}}$ | 387 K | $\kappa_z^2$ | $14.12\times10^{-16}$ m$^2$ |
| $v$ | $1\times10^{-8}$ m s$^{-1}$ | $W$ | $6.878\times10^{3}$ |
| $\delta$ | $1\times10^{-9}$ m | $\zeta$ | 0.256 |
| $\sigma_{x,y}{}^{\mathrm{a,b}}$ | 0.0137 J m$^{-2}$ | | |
| $\sigma_z{}^{\mathrm{a,b}}$ | 0.09 J m$^{-2}$ | | |

[a] For solvated PE crystals [7].

[b] The surface energies are approximated as $\sigma_{x,y}=\sigma_l$, $\sigma_z=\sigma_e$, $\sigma_l=0.0137$ J m$^2$, and $\sigma_e=0.09$ J m$^2$ [7].

existing single crystal surface. However, the present theoretical model is not designed to account for the multilayer growth of single crystal mats.

### C. Curved single crystal in polyethylene

Another interesting feature in polymer crystallization is the growth of curved single crystals. The curved crystals in polyethylene are formed by growth along six growth fronts: two normal to the $(\bar{1}\bar{1}0)$ and $(110)$ planes, and two normal to the $a$ axis [along the (100) plane]. In this paper, we propose that the growth along these various crystallographic planes can be modeled simply by employing different values of $\kappa$ normal to these planes. The interface gradient coefficient tensor in dimensionless units $\tilde{\kappa}$ can be written as sum of the corresponding tensors for the two growth fronts, viz.,

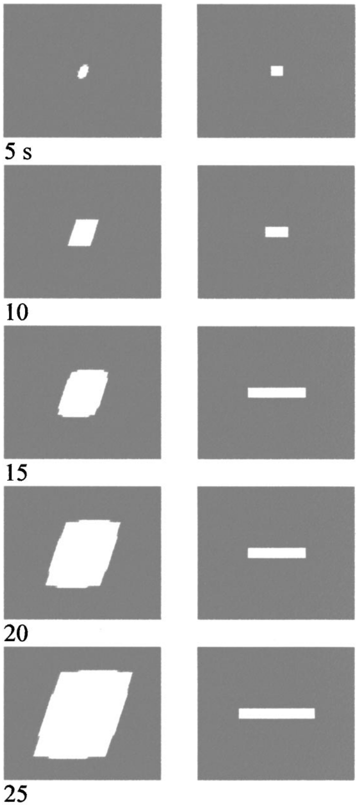

FIG. 10. The spatiotemporal growth of a polyethylene crystal in the crystal order parameter field calculated according to Eq. (21), with the coefficients listed in Table II. The simulated patterns in the first column represent the diamond shaped single crystal in the $x$-$y$ plane, whereas those in the second column show the lamellar thickness in the $x$-$z$ cross section. The simulations were carried out on a $64\times64\times64$ lattice.

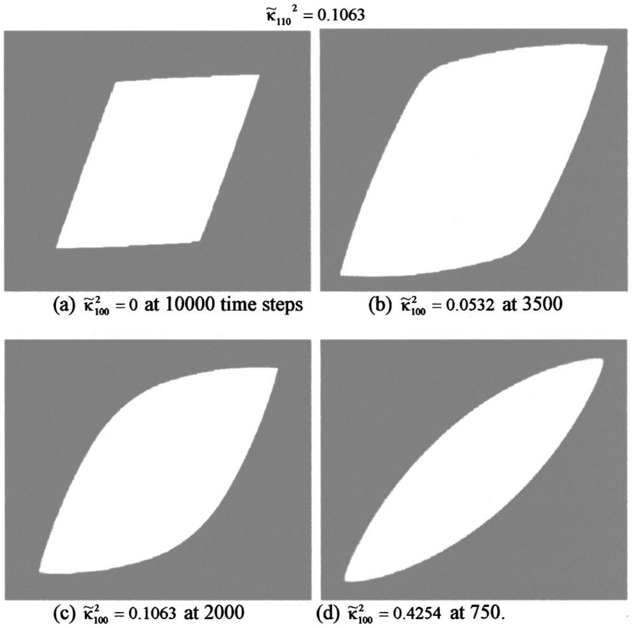

(a) $\tilde{\kappa}^2_{100} = 0$ at 10000 time steps (b) $\tilde{\kappa}^2_{100} = 0.0532$ at 3500

(c) $\tilde{\kappa}^2_{100} = 0.1063$ at 2000 (d) $\tilde{\kappa}^2_{100} = 0.4254$ at 750.

FIG. 11. The simulated curved crystals in the crystal order parameter field according to Eq. (24), with $\tilde{\Gamma}=0.1894$, $W=5.086$, $\zeta=0.256$, and $\tilde{\kappa}^2_{110}=0.1063$, showing various topologies of curved single crystals: (a) a diamond shaped single crystal, (b) a lozenge shaped curved single crystal, (c) a lenticular curved single crystal, and (d) a slender curved single crystal.

$$\tilde{\boldsymbol{\kappa}}=\tilde{\boldsymbol{\kappa}}^{ij}_{110}+\boldsymbol{\alpha}^{*i}_{p}\boldsymbol{\alpha}^{*j}_{q}\tilde{\boldsymbol{\kappa}}^{pq}_{100}, \tag{23}$$

where $\tilde{\kappa}_{110}=\left\{\begin{matrix}\tilde{\kappa}_{110} & 0\\ 0 & \tilde{\kappa}_{110}\end{matrix}\right\}$ and $\tilde{\kappa}_{100}=\left\{\begin{matrix}\tilde{\kappa}_{100} & 0\\ 0 & 0\end{matrix}\right\}$; $i,j,p,q=1,2$.

The second term in Eq. (23) is simply the coordinate transformation from the $a$-$b$ coordinate to the $x$-$y$ coordinate with a transformation tensor given as

$$\boldsymbol{\alpha}=\frac{a^2+b^2}{4a^2}\left\{\begin{matrix}1 & -1\\ -1 & 1\end{matrix}\right\}.$$

The governing equation in the dimensionless form is thus

$$\frac{\partial\psi}{\partial\tau}=-\tilde{\Gamma}[W\psi(\psi-1)(\psi-\zeta)-\tilde{\boldsymbol{\nabla}}\cdot\{\tilde{\boldsymbol{\kappa}}\cdot(\tilde{\boldsymbol{\kappa}}\cdot\tilde{\boldsymbol{\nabla}}\psi)\}], \tag{24}$$

where the derivation of $\tilde{\boldsymbol{\nabla}}\cdot[\tilde{\boldsymbol{\kappa}}\cdot(\tilde{\boldsymbol{\kappa}}\cdot\tilde{\boldsymbol{\nabla}}\psi)]$ is the same as that in real dimensions given by Eq. (A9) in the Appendix.

Equation (24) has been solved to investigate the effect of the relative values of $\tilde{\kappa}_{100}$ and $\tilde{\kappa}_{110}$ on the shape of the growing single crystal (Fig. 11) by varying the values of $\tilde{\kappa}_{100}$ while keeping the value of $\tilde{\kappa}_{110}$ constant. When $\tilde{\kappa}_{100}$ is zero, one obtains a diamond-shaped crystal [Fig. 11(a)], as discussed in Sec. III B. When $\tilde{\kappa}_{100}<\tilde{\kappa}_{110}$, the shape is that of the curved crystal with smooth and serrated edges, i.e., the growth front along the four (110) planes is smooth and flat, while that along the two (100) planes is serrated and hence curved [Fig. 11(b)]. These features are in good accord with the observed PE single crystals [8] as well as that simulated by Miller and Hoffman [11,12]. The advantage of the present approach is that it is unnecessary to treat the growth sectors differently as done by Miller and Hoffman [11,12], who considered the growth of the (110) sector to be governed by the flat edge mechanism and the (100) front to be serrated on the molecular level. Simple relative values of $\tilde{\kappa}_{100}$ and $\tilde{\kappa}_{110}$ appear sufficient to generate various topologies encompassing diamond-shaped to lenticular and curved single crystals with straight and/or serrated edges. When $\tilde{\kappa}_{100}=\tilde{\kappa}_{110}$, a lenticular crystal emerges [Fig. 11(c)]. Moreover, if $\tilde{\kappa}_{100}>\tilde{\kappa}_{110}$, then slender single crystals emerge [Fig. 11(d)]; thus it is in good agreement with the morphology reported by Point and Villers [15]. It is seen that the number of time steps required to reach comparable sizes of the single crystals decreases with an increasing $\tilde{\kappa}_{100}$ value.

### D. Conclusions

The spatiotemporal evolution of the nonconserved crystal order parameter based on the TDGL model A shows faceted single crystal growth with the features reminiscent of regime I, i.e., the spreading of the stems on the lamellar strip. However, a new stem could be deposited on the newly formed strip before all the sites are fully filled, particularly when the size of the single crystal becomes large. That is to say when the nucleation controlled growth rate *G*, is close to the lateral growth rate *g*, there is a crossover in behavior from regime I to regime II. The front edge becomes serrated and eventually evolves to a curved crystal. The total free energy density decays in a rhythmic manner in synchronism with the nucleation event, i.e., the monotonic decay of the free energy during growth is raised periodically by the excess free energy associated with each nucleation event on the newly formed lamellar strips. The simulation with the tensor forms of the interface gradient coefficients based on the TDGL model A captures the emergence of various topologies encompassing square, rectangular, diamond-shaped, and curved single crystals. In 3D simulations, the single crystal grows exclusively by spreading in the lateral sides as compared to that in the thickness direction due to the high penalty for nucleation to occur on the folded lamellar surface relative to the sides. It should be emphasized that the aforementioned crystal growth behavior cannot be accounted for by regular front propagation models such as the classical Fisher-Kolmogorov equation or its modifications [17], as these equations lack metastability for nucleation.

## ACKNOWLEDGMENT

Support of this work by the NSF through Grant No. DMR 9903519 is gratefully acknowledged.

## APPENDIX: DERIVATION OF FUNCTIONAL DERIVATIVE $\delta F/\delta\psi$

The functional derivative $\delta F/\delta\psi$ may be expanded in accordance with the well-known identity relation of Lagrangian mechanics [39]:

$$\frac{\delta F}{\delta\psi}=\frac{\partial f_{\mathrm{cryst}}}{\partial\psi}-\nabla\frac{\partial f_{\mathrm{cryst}}}{\partial\nabla\psi}. \tag{A1}$$

The first term may be decomposed as

$$\frac{\partial f_{\mathrm{cryst}}}{\partial\psi}=\frac{\partial f_{\mathrm{local}}}{\partial\psi}+\frac{\partial f_{\mathrm{grad}}}{\partial\psi},$$

and, using Eq. (4), gives

$$\begin{aligned}\frac{\partial f_{\mathrm{cryst}}}{\partial\psi}&=\frac{\partial f_{\mathrm{local}}}{\partial\psi}+\frac{\partial}{\partial\psi}\left[\frac{1}{2}(\boldsymbol{\kappa}\cdot\boldsymbol{\nabla}\psi)^2\right]\\&=\frac{\partial f_{\mathrm{local}}}{\partial\psi}+(\boldsymbol{\kappa}\cdot\nabla\psi)\cdot\left(\boldsymbol{\kappa}\cdot\frac{\partial}{\partial\psi}\nabla\psi+\nabla\psi\cdot\frac{\partial}{\partial\psi}\boldsymbol{\kappa}\right).\end{aligned}$$

Assuming $\boldsymbol{\kappa}$ to be independent of $\psi$, one obtains

$$\frac{\partial f_{\mathrm{cryst}}}{\partial\psi}=\frac{\partial f_{\mathrm{local}}}{\partial\psi}. \tag{A2}$$

On the other hand, the second term of Eq. (A1) may be deduced further as follows:

$$\begin{aligned}\frac{\partial f_{\mathrm{cryst}}}{\partial\nabla\psi}&=\frac{\partial f_{\mathrm{local}}}{\partial\nabla\psi}+\frac{\partial}{\partial\nabla\psi}\left[\frac{1}{2}(\boldsymbol{\kappa}\cdot\boldsymbol{\nabla}\psi)^2\right]\\&=\left[\frac{\partial}{\partial\nabla\psi}(\boldsymbol{\kappa}\cdot\boldsymbol{\nabla}\psi)\right]\cdot(\boldsymbol{\kappa}\cdot\boldsymbol{\nabla}\psi)\\&=\left(\frac{\partial\nabla\psi}{\partial\nabla\psi}\boldsymbol{\kappa}+\nabla\psi\frac{\partial\boldsymbol{\kappa}}{\partial\nabla\psi}\right)\cdot(\boldsymbol{\kappa}\cdot\boldsymbol{\nabla}\psi)=\boldsymbol{\kappa}\cdot(\boldsymbol{\kappa}\cdot\boldsymbol{\nabla}\psi).\end{aligned}$$

Hence

$$\nabla\frac{\partial f_{\mathrm{cryst}}}{\partial\nabla\psi}=\boldsymbol{\nabla}\cdot[\boldsymbol{\kappa}\cdot(\boldsymbol{\kappa}\cdot\nabla\psi)]. \tag{A3}$$

From Eq. (3), we have

$$\frac{\partial f_{\mathrm{local}}}{\partial\psi}=W\psi(\psi-1)(\psi-\zeta). \tag{A4}$$

Substituting Eqs. (A2), (A3), and (A4) into Eq. (A1) gives

$$\frac{\delta F}{\delta\psi}=W\psi(\psi-1)(\psi-\zeta)-\boldsymbol{\nabla}\cdot[\boldsymbol{\kappa}\cdot(\boldsymbol{\kappa}\cdot\nabla\psi)]. \tag{A5}$$

Substituting Eq. (A5) into Eq. (1) leads to the governing equation, i.e.,

$$\frac{\partial\psi}{\partial t}=-\Gamma\frac{\delta F}{\delta\psi}=-\Gamma\{W\psi(\psi-1)(\psi-\zeta)-\boldsymbol{\nabla}\cdot[\boldsymbol{\kappa}\cdot(\boldsymbol{\kappa}\cdot\boldsymbol{\nabla}\psi)]\}, \tag{A6}$$

thereby recovering Eq. (6).

The term $\boldsymbol{\nabla}\cdot[\boldsymbol{\kappa}\cdot(\boldsymbol{\kappa}\cdot\nabla\Psi)]$ in Eq. (A6) is further given by the expression

$$\begin{aligned}\boldsymbol{\nabla}\cdot[\boldsymbol{\kappa}\cdot(\boldsymbol{\kappa}\cdot\boldsymbol{\nabla}\psi)]&=\boldsymbol{\nabla}\cdot\left\{\boldsymbol{\kappa}\cdot\left[\boldsymbol{\kappa}\cdot\left(\frac{\partial\psi}{\partial x^j}\hat{e}^j\right)\right]\right\}\quad\text{for } j=1,2\\&=\boldsymbol{\nabla}\cdot\left[\boldsymbol{\kappa}\cdot\left(\kappa^{ij}\frac{\partial\psi}{\partial x^j}\hat{e}_j\right)\right]\quad\text{for } i=1,2\\&=\boldsymbol{\nabla}\cdot\left(\kappa^{mn}\gamma_{ni}\kappa^{ij}\frac{\partial\psi}{\partial x^j}\hat{e}_i\right)\quad\text{for } m,n=1,2,\end{aligned}\tag{A7}$$

$$\boldsymbol{\nabla}\cdot[\boldsymbol{\kappa}\cdot(\boldsymbol{\kappa}\cdot\boldsymbol{\nabla}\psi)]=\kappa^{mn}\kappa^{ij}\gamma_{ni}\frac{\partial^2\psi}{\partial x^m\,\partial x^j},$$

where $\hat{e}^x,\hat{e}^y$ and $\hat{e}_i,\hat{e}_j$ are covariant and contravariant unit vectors in $x$ and $y$ directions:

$$\begin{cases}\gamma_{ij}=1 & \text{if } i=j,\\ \gamma_{ij}=\cos(\alpha) & \text{if } i\neq j.\end{cases}\tag{A8}$$

Since $\cos(\alpha)=0$, the metric tensor $\gamma$ in the rhomboidal lattice becomes a Kronecker $\delta$ in the square lattice. If the tensor $\boldsymbol{\kappa}$ is taken such that $\kappa_{21}=\kappa_{12}$ and $\kappa_{11}=\kappa_{22}$ then Eq. (A6) can be expanded as

$$\begin{aligned}\nabla\cdot[\boldsymbol{\kappa}\cdot(\boldsymbol{\kappa}\cdot\nabla\psi)]=&[(\kappa_{11})^2+(\kappa_{12})^2+2\cos(\alpha)\kappa_{11}\kappa_{12}]\\&\times\left(\frac{\partial^2\psi}{\partial^2 x}+\frac{\partial^2\psi}{\partial^2 y}\right)+2\{2\kappa_{11}\kappa_{12}+\cos(\alpha)\\&\times[(\kappa_{11})^2+(\kappa_{12})^2]\}\frac{\partial^2\psi}{\partial x\,\partial y}.\end{aligned}\tag{A9}$$

In a specific case where $\kappa_{21}=\kappa_{12}=0$ and $\kappa_{11}=\kappa_{22}=\kappa$, Eq. (A6) leads to Eq. (11), i.e.,

$$\frac{\partial\psi}{\partial t}=-\Gamma\left[W\psi(\psi-1)(\psi-\zeta)-\kappa^2\nabla^2\psi-2\cos(\alpha)\kappa^2\frac{\partial^2\psi}{\partial x\,\partial y}\right].\tag{A10}$$

It should be noted that the present derivation is valid for the dimensionless case, i.e., the same as the renormalized coefficient of interface gradient term in Eq. (24).

[1] P. H. Geil, *Polymer Single Crystals*, 2nd ed. (Wiley, New York, 1963).
[2] *Treatise On Solid State Chemistry*, edited by N. B. Hannay (Plenum, New York, 1976), Vol. 3.
[3] D. C. Bassett, *Principles of Polymer Morphology* (Cambridge University Press, Cambridge, 1981).
[4] G. Strobl, *The Physics of Polymers* (Springer-Verlag, Berlin, 1996).
[5] K. Armistead and G. Goldbeck-Wood, Adv. Polym. Sci. **100**, 219 (1992).
[6] J. L. Lauritzen and J. D. Hoffman, J. Chem. Phys. **31**, 1680 (1959); J. Res. Natl. Bur. Stand., Sect. A **65**, 297 (1961).
[7] J. D. Hoffman, G. T. Davis, and J. I. Lauritzen, Jr., in *Treatise on Solid State Chemistry* (Ref. [2]), Chap. 7, p. 497.
[8] F. Khoury and E. Passaglia, in *Treatise on Solid State Chemistry* (Ref. [2]), Chap. 6, p. 335; E. Passaglia and F. Khoury, Polymer **25**, 631 (1984).
[9] D. M. Sadler, Polymer **25**, 1446 (1984); **28**, 1440 (1987).
[10] M. L. Mansfield, Polymer **29**, 1755 (1988).
[11] J. D. Hoffman and R. L. Miller, Macromolecules **22**, 3038 (1989).
[12] R. L. Miller and J. D. Hoffman, Polymer **32**, 963 (1991).
[13] F. C. Frank, J. Cryst. Growth **22**, 233 (1974).
[14] Y. Tanzawa and A. Toda, Polymer **37**, 1621 (1996).
[15] J. J. Point and D. Villers, Polymer **33**, 2263 (1992).
[16] D. C. Bassett, R. H. Olley, and A. M. Al Raheil, Polymer **29**, 1539 (1988).
[17] X. Y. Wang, S. Fan, and T. Kyu, Phys. Rev. E **56**, 4931 (1997), and references therein.
[18] L. D. Landau, Phys. Z. Sowjetunion **11**, 26 (1937); reprinted in *Collected Papers of L. D. Landau*; edited by D. ter Haar (Pergamon, New York, 1965).
[19] J. S. Langer, in *Directions in Condensed Matter Physics*, edited by G. Grinstein and G. Mazenko (World Scientific, Singapore, 1986), p. 164.
[20] G. Caginalp and E. A. Sokolovsky, Appl. Math. Lett. **2**, 117 (1989); G. Caginalp, Phys. Rev. A **39**, 5887 (1989).
[21] G. Caginalp and P. C. Fife, Phys. Rev. B **33**, 7792 (1986); O. Penrose and P. C. Fife, Physica D **43**, 44 (1990).
[22] R. Kobayashi, Physica D **63**, 410 (1993).
[23] A. A. Wheeler, W. J. Boettinger, and G. B. McFadden, Phys. Rev. A **45**, 7424 (1992).
[24] E. Fried and M. E. Martin, Physica D **91**, 143 (1996).
[25] M. Fabbri and V. R. Voller, J. Comput. Phys. **130**, 256 (1997).
[26] B. I. Halperin, P. C. Hohenberg, and S. K. Ma, Phys. Rev. B **10**, 139 (1974).
[27] J. D. Gunton, M. San Miguel, and P. S. Sahni, in *Phase Transitions and Critical Phenomena*, edited by C. Domb and J. L. Lebowitz (Academic, New York, 1983), p. 267.
[28] K. R. Elder, F. Drolet, J. M. Kosterlitz, and M. Grant, Phys. Rev. Lett. **72**, 677 (1994).
[29] T. Kyu, H.-W. Chiu, A. J. Guenthner, Y. Okabe, H. Saito, and T. Inoue, Phys. Rev. Lett. **83**, 2749 (1999).
[30] O. Olabisi, L. M. Robeson, and M. T. Shaw, *Polymer-Polymer Miscibility* (Academic, New York, 1979).
[31] J. W. Cahn and J. E. Hilliard, J. Chem. Phys. **28**, 258 (1958).
[32] See, *Treatise on Solid State Chemistry* (Ref. [2]), p. 379; F. Khoury and J. D. Barnes, J. Res. Natl. Bur. Stand., Sect. A **76**, 225 (1972).
[33] M. J. Grimson and G. C. Barker, Phys. Rev. E **49**, 1680 (1994).
[34] B. Lotz, A. J. Lovinger, and R. E. Cais, Macromolecules **21**, 2375 (1988).
[35] Z. Bu, Y. Yoon, R.-M. Ho, W. Zhou, I. Jangchud, R. K. Eby, S. Z. D. Cheng, E. T. Hsieh, T. W. Johnson, R. G. Geerts, S. J. Palackal, G. R. Hawley, and M. B. Welch, Macromolecules **29**, 6575 (1996).
[36] A. Keller and S. Z. D. Cheng, Polymer **39**, 4401 (1998).
[37] S. M. Allen and J. W. Cahn, Metallurgica **27**, 1085 (1979).
[38] P. R. Harowell and D. W. Oxtoby, J. Chem. Phys. **86**, 2932 (1987).
[39] P. N. Chaikin and T. C. Lubenski, *Principles of Condensed Matter Physics* (Cambridge University Press, Cambridge, 1995), p. 142.